A Mobile Sensing System for Structural Health Monitoring: Design and Validation

Dapeng Zhu[1], Xiaohua Yi[1], Yang Wang[1,3], Kok-Meng Lee[2] and Jiajie Guo[2]

[1] School of Civil and Environmental Engineering, Georgia Institute of Technology, Atlanta, GA 30332, USA
[2] School of Mechanical Engineering, Georgia Institute of Technology, Atlanta, GA 30332, USA

E-mail: yang.wang@ce.gatech.edu

Abstract. This paper describes a new approach of using mobile sensor networks for structural health monitoring. Compared with static sensors, mobile sensor networks offer flexible system architectures with adaptive spatial resolutions. The paper first describes the design of a mobile sensing node that is capable of maneuvering on structures built with ferromagnetic materials. The mobile sensing node can also attach/detach an accelerometer onto/from the structural surface. The performance of the prototype mobile sensor network has been validated through laboratory experiments. Two mobile sensing nodes are adopted for navigating on a steel portal frame and providing dense acceleration measurement. Transmissibility function analysis is conducted to identify structural damage using data collected by the mobile sensing nodes. This preliminary work is expected to spawn transformative changes of using mobile sensors for future structural health monitoring.

1. Introduction

The deterioration of civil infrastructure systems has attracted much public attention in recent years, partly due to a number of catastrophic events that have been widely covered by the media. In the United States, more than half of the bridges were built before 1940's, and more than one in four of the bridges were categorized as structurally deficient or functionally obsolete [1]. It was estimated that a $17 billion annual investment is needed to substantially improve current bridge conditions, yet currently, only $10.5 billion is spent annually on the construction and maintenance of bridges. Due to the lack of funding for timely retrofitting, average condition of the bridges in the US is expected to continue deteriorating in the foreseeable future. In order to efficiently utilize the limited resources, a need-based scheduling for bridge retrofitting should be established based upon the actual condition of individual bridges.

To assess the condition of bridges, current U.S. federal highway administration (FHWA) requests local transportation authorities to visually inspect the entire inventory of over 600,000 highway bridges. The inspections are usually conducted biennially, which may not be timely enough for capturing rapidly growing damage. Shown by a FHWA study, visual inspections are highly subjective; significantly different condition ratings can be given for the same bridge by different

[3] Author to whom any correspondence should be addressed.

inspectors [2]. Furthermore, visual inspections can only identify damage that is visible on the structural surface; damage located below the surface often remains unrevealed. As a result, there is a pressing need for reliable structural monitoring systems that can automatically and quantitatively assess the real-time condition of civil structures.

As a complimentary approach and promising alternative to structural inspections, recent years have seen increasing research interest in structural health monitoring (SHM). A SHM system measures structural performance and operating conditions with various types of sensing devices, and evaluates structural conditions using certain damage diagnosis or prognosis algorithms [3, 4]. Among the many advances in SHM research, "smart" wireless sensors capable of embedded computing and wireless communication have been highly attractive. Wireless communication in SHM systems was originally proposed to significantly reduce the monetary and time cost for installing lengthy cables in a SHM system [5]. A great amount of efforts have been made in exploring wireless sensing systems for structural health monitoring [6-9]. For example, the wireless SHM platform in [10] has been successfully validated on a number of bridges, buildings, and wind turbines located in the US, Taiwan, South Korea, China, and Germany [11-13].

Besides wireless sensing, the next revolution in sensor networks has been predicted to be mobile sensor networks that implant mobility into traditional sensor networks [14, 15]. In a mobile sensor network, each mobile sensing node can be a miniature mobile robot equipped with smart sensors. The mobile sensing node explores its surroundings and exchanges information with its peers through wireless communication. The mobility of a sensing node resolves some most critical challenges faced by static wireless sensor networks [16]: (i) In order to closely monitor a complex large-scale structure, static wireless sensors usually need to be deployed at a very high density. However, the cost and difficulty associated with dense arrays of wireless sensors are still prohibitive for wide deployment in practice. On the other hand, mobile sensor networks offer flexible architectures, which lead to adaptive and high spatial resolutions while using a relatively small number of nodes. (ii) Limited power supply is one of the largest constraints for wireless sensor networks. This constraint is eliminated in mobile sensor networks, if the mobile sensing nodes can periodically return to a base station for automatic recharging. (iii) For mobile sensor networks, reduced power constraint means that powerful microprocessors can be adopted to execute more sophisticated damage detection algorithms; it also enables more options for wireless transceivers that offer higher data rate, longer transmission range, and better synchronization accuracy.

Motivated by the interest to incorporate mobility into traditional sensors, some inspection robots have been developed for SHM. For example, a robot able to crawl on a 2D surface was developed for visually inspecting aircraft exterior; the robot used ultrasonic motors for mobility and suction cups for adherence [17]. A beam-crawler has been developed for wirelessly powering and interrogating battery-less peak-strain sensors; the crawler moves along the flange of an I-beam by wheels [18]. Based upon magnetic on-off robotic attachment devices, a magnetic walker has been developed for maneuvering on a 2D surface [19]. Most recently, a remotely-controlled model helicopter has been illustrated for charging and communicating with wireless sensors [20]. However, to the best of our knowledge, mobile sensor networks with dynamic reconfiguration have rarely been explored by researchers for SHM purpose.

This research aims to explore mobile sensor networks for structural health monitoring. Our previous prototype mobile SHM system adopted magnet-wheeled robots as the sensor carriers [21]. These mobile sensing nodes can maneuver upon structures built with ferromagnetic/steel materials. In our first prototype, accelerometers on each mobile sensing node are not in direct contact with the steel structure; therefore, higher frequency components in the structural vibration cannot be accurately captured for detecting local damage. In order to improve the performance, a second prototype mobile SHM system has been recently developed [22, 23]. This paper presents in detail the development and validation of the second prototype mobile sensing system, which is capable of attaching an accelerometer to structural surface for high-precision measurement. The paper begins with the mechatronic hardware and software implementation of the mobile sensing nodes, which is followed by

a brief introduction to transmissibility function analysis. Validation experiments for the mobile sensing node are then presented. Two damage scenarios are investigated, the first scenario simulated with an extra mass block, and the second scenario simulated with loosened bolts. Using acceleration data collected by the mobile sensors, transmissibility function analysis [24-27] is conducted for damage detection and localization.

2. Design of the mobile sensing node

The mobile sensing system contains a computer server and multiple mobile sensing nodes that communicate with each other through a wireless network. Each mobile sensing node has its own power supply and is completely tetherless. The computer server sends various commands (such as navigation, data collection, or embedded computing) to the mobile sensing nodes through wireless communication. The mobile sensing nodes then perform the required actions. The design of the mobile sensing node is based upon a previously developed wireless sensing unit, and entails efforts in mechanical, hardware, and software design. Detailed description of the wireless sensing unit and associated validation work can be found in [10-13]. The cost of each mobile sensing node is about a few hundred dollars. Compared with a typical cable-based structural monitoring system with cabled channels that usually cost a few thousand dollars per channel [28], mobile sensing offers a potential approach to significantly reduce the total cost of an SHM system. Built upon the wireless sensing unit, significant progress is accomplished in order to enable mobility of the sensing node. This section first introduces the mechanical design of the prototype mobile sensing node, and then describes the electronic hardware and software design.

2.1. Mechanical design

Figure 1 shows the picture of the prototype mobile sensing node that consists of three major parts: two 2-wheel cars and a compliant beam connecting the two cars. Each 2-wheel car contains a body frame, two motors, two 9V batteries, a wireless sensing unit [10], two infrared (IR) sensors, two Hall effect sensors, as well as auxiliary circuits. The mobile sensing node maneuvers with four motorized wheels, two of which belong to each car. Every wheel is surrounded by thin rectangular magnets (magnetized along the thickness direction) to provide attraction between the wheel and the surface of the underlying ferromagnetic structure. Two 9V batteries are placed on each 2-wheel car, underneath the wireless sensing unit. One battery powers the two motors and the other powers the electronic circuits in the car. Each Hall effect sensor measures the angular velocity of a wheel, while each IR sensor detects the boundary of the underlying structural surface.

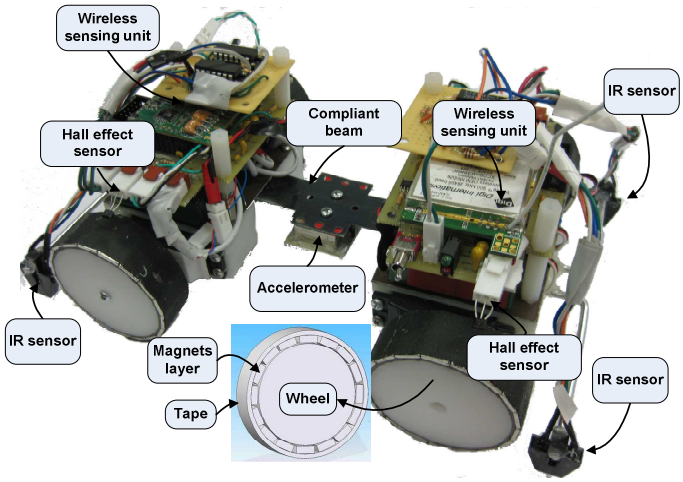

Figure 1. Picture of the mobile sensing node.

A Silicon Designs 2260-010 accelerometer is mounted at the center of the compliant beam between the two 2-wheel cars. Materials with high flexibility can be adopted for constructing the compliant beam, such as spring steel or polyoxymethylene plastic (aka. brand name Delrin). When acceleration measurement is to be made, the accelerometer can be attached onto the underlying structural surface by bending the center of compliant beam towards the surface (Figure 2a); this bending is achieved by commanding the two cars move towards each other. Small-size magnet blocks are arranged around the center of the compliant beam, in order to firmly hold down the accelerometer onto the structural surface. On the other hand, the accelerometer can be detached from the surface by straightening the compliant beam after measurement (Figure 2b); this straightening is achieved by commanding the two cars to move away from each other. After the accelerometer is detached, the mobile sensing node resumes its mobility and can move to next location for another measurement. As shown in Figure 2(c), the flexibility of the compliant beam also assists when the mobile sensing node transits between two structural members.

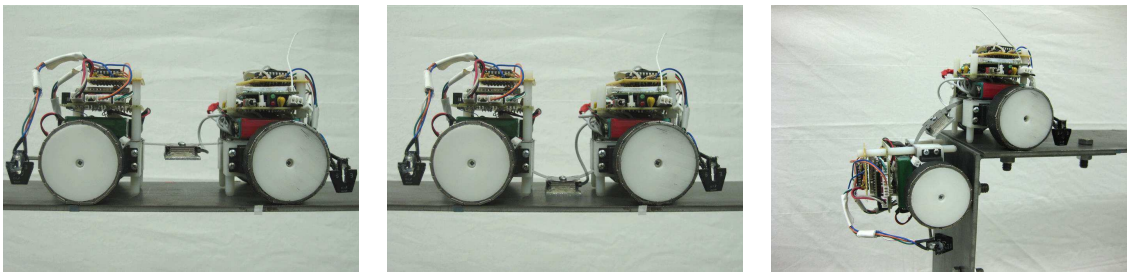

(a) (b) (c)

Figure 2. Side view of the magnet-wheeled mobile sensing node: (a) sensor attachment; (b) sensor detachment; (c) transition over a right angle.

The width of the mobile sensing node is about 0.152m (6 in), and the height is about 0.091m (3.6 in). When the sensor is attached to the structural surface, the length of the mobile sensing node is 0.191m (7.5 in). When the sensor is detached, the length of the node is 0.229 m (9 in). The overall weight of the mobile sensing node (including two cars) is about 1 kg (2.2 lbs), most of which is contributed by the magnet wheels, motors, and batteries.

2.2. Functional modules

Figure 3 illustrates the functional diagram of the mobile sensing node that consists of two 2-wheel cars. Each 2-wheel car contains one wireless sensing unit, an additional mobility module, and various sensor modules. In particular, each wireless sensing unit consists of three sub-modules: sensor signal

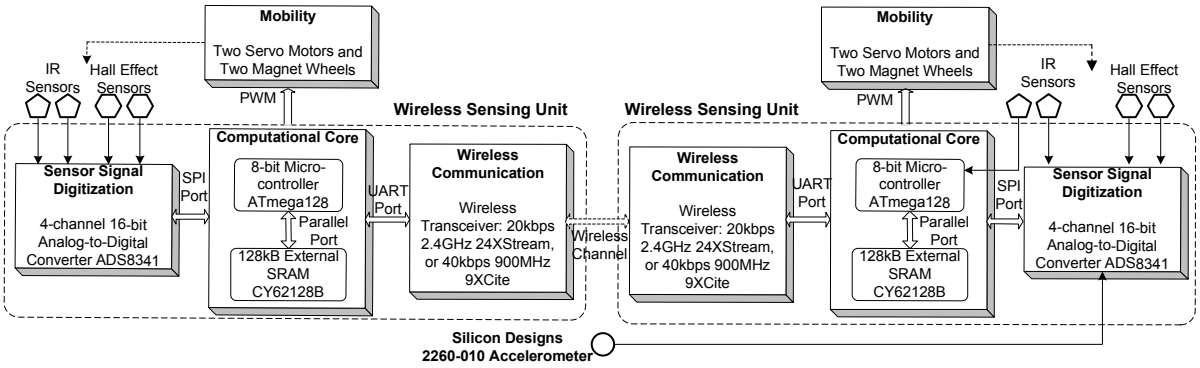

Figure 3. Functional diagram of the mobile sensing node consisting of two cars, left half of the diagram corresponding to components in one car and right half corresponding to another car.

digitization, computational core, and wireless communication. (i) The sensing interface, which is mainly provided by a 16-bit analog-to-digital (A/D) converter (Texas Instrument ADS8341), converts four channels of analog sensor signals into digital data which is then transferred to the computational core through a high-speed Serial Peripheral Interface (SPI) port. Sources of the sensor signals include the accelerometer, the Hall effect sensors, and the IR sensors. (ii) The ATmega128 microcontroller and the external Static Random Access Memory (SRAM) CY62128B together constitute the computational core that performs local data storage and analysis. In addition, each Atmel ATmega128 microcontroller provides eight 10-bit A/D channels, which have lower resolution than the ADS8341 A/D conversion. (iii) The computational core communicates with a MaxStream wireless transceiver through a Universal Asynchronous Receiver and Transmitter (UART) interface. Using the wireless communication channel, each wireless unit can exchange information with other units, or with the computer server.

Figure 3 also shows that each car has a mobility module that consists of two server motors and two magnet wheels. In order to enable mobility, each ATmega128 microcontroller commands two servo motors with pulse-width-modulation (PWM) signals generated through the timer interrupt functions of the microcontroller. The speed and direction of each motor are controlled by the duty cycle of the PWM signal. When the mobile sensing node is moving, real-time motion is monitored by the IR sensors and Hall effect sensors, and the motion information is instantly transferred to the microcontroller for feedback control.

Using typical 9V batteries, the mobile sensing node is able to operate for about half an hour; work is under way to replace the 9V batteries with higher-capacity Lithium-ion batteries for an operational life of at least a few hours. For future field deployment, an on-site shelter can be constructed for storing and automatically recharging the mobile node through inductive coupling. In addition, it should be noted that the current prototype mobile node (particularly the electronics) is not water-proof, and therefore, cannot operate safely in harsh outdoor conditions.

2.3. Mobility

To offer reliable mobility, one important criterion is to make four wheels of the mobile node stay synchronized during movement. In other words, all four wheels should have the same angular velocities during movement, although each wheel is actuated by an individual motor. To accurately orchestrate the wheel angular velocities, real-time feedback control is implemented. One Hall effect sensor, which is capable of measuring the flux of a magnetic field, is placed upon each magnet wheel. In the current prototype, sixteen small-size thin magnets are placed around the wheel with alternating

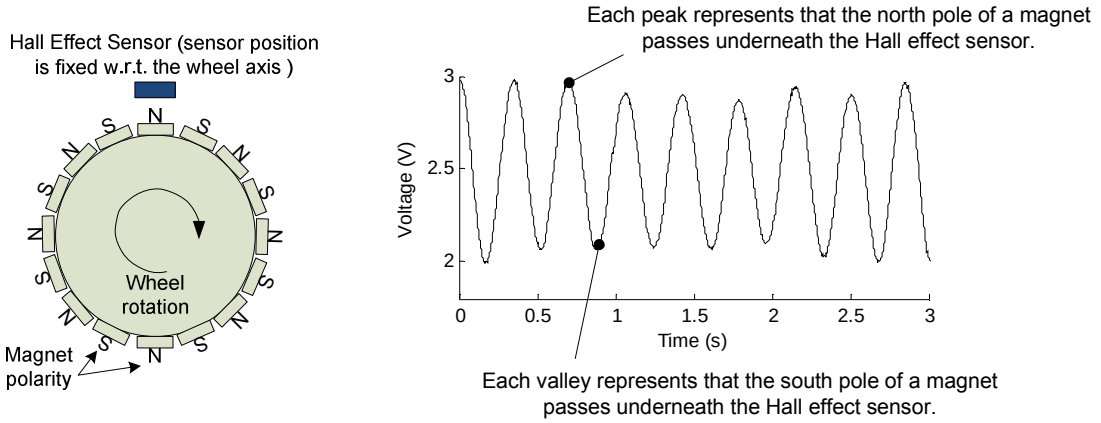

(a) (b)

Figure 4. A Hall effect sensor measuring wheel rotation: (a) sensor is placed above a rotating magnet wheel; (b) the output signal of the Hall effect sensor when the magnet wheel rotates.

polarities (Figure 4a). When the wheel rotates, the alternating polarities cause the magnet flux density measured by the Hall effect sensor to change periodically. Figure 4(b) illustrates typical voltage output of the Hall effect sensor when the mobile sensing node moves. During each period, two neighboring magnets pass underneath the Hall effect sensor. As a result, the output signal from the Hall effect sensor can be used to estimate the angular velocity of the wheel, so that the velocity data is fed back to the microcontroller in real time for synchronizing the four wheels. The feedback control is conducted through classic proportional–integral–derivative (PID) controllers operating at 20Hz sampling rate.

To ensure that the mobile sensing node moves safely on an underlying structural surface, infrared (IR) sensors are placed at both sides of the front 2-wheel car, as well as both sides of the rear 2-wheel car, for boundary detection. In each IR sensor, an emitting diode emits infrared radiation, and a detection diode detects the radiation reflected from the structural surface. When the sensing node moves outside the surface boundary, less IR signal will be reflected to the detection diode. To make the mobile sensing node stay within the boundaries of the underlying structural surface, both microcontrollers in the mobile node need real-time data from the IR sensors of the front car. For example, when the front 2-wheel car detects that its left wheel is moving out of boundary, the left wheels of both cars are immediately accelerated (or the right wheels of both cars are decelerated) to correct the movement direction. Peer-to-peer communication between the wireless sensing units on the two cars is used for exchanging boundary detection information in real time.

3. Transmissibility function analysis

This section briefly introduces the general definition of transmissibility function. A damage indicator for detecting and localizing damage is then described, followed by the definition of a repeatability indicator for quantifying the experimental uncertainties.

3.1. Introduction to transmissibility function

Many vibration-based methods have been developed for structural damage detection [29]. Among these methods, transmissibility function analysis has attracted considerable attention because of its effectiveness in identifying damage using output data only [24-27].

The equations of motion for an n-degree-of-freedom (n-DOF) linear structure can be formulated as:

$$\mathbf{M}\ddot{\mathbf{x}}(t) + \mathbf{C}\dot{\mathbf{x}}(t) + \mathbf{K}\mathbf{x}(t) = \mathbf{f}(t) \tag{1}$$

where $\mathbf{x}(t)$ is the $n\times1$ displacement vector, $\mathbf{M}$ is the $n\times n$ mass matrix, $\mathbf{C}$ is the $n\times n$ viscous damping matrix, $\mathbf{K}$ is the $n\times n$ stiffness matrix, and $\mathbf{f}(t)$ is the $n\times1$ input force vector. If the input force is only applied to the k-th DOF, then $\mathbf{f}(t) = \{0_1, 0_2, \ldots, f_k(t),\ldots, 0_n\}^{\mathrm{T}}$ has only one non-zero entry.

Equation (1) can be represented in frequency domain as:

$$\mathbf{X}(\omega) = \mathbf{H}(\omega)\mathbf{F}(\omega) \tag{2}$$

where $\mathbf{H}(\omega) = \left(\mathbf{K} - \omega^2\mathbf{M} + \mathrm{i}\omega\mathbf{C}\right)^{-1}$ is the $n\times n$ frequency response function (FRF) matrix. Assuming the input force is only applied to the k-th DOF, the input force vector in frequency domain is determined as:

$$\mathbf{F}(\omega) = \{0_1, 0_2, \ldots, F_k(\omega),\ldots, 0_n\}^{\mathrm{T}} \tag{3}$$

The acceleration vector in the frequency domain can be formulated as:

$$\mathbf{A}(\omega) = -\omega^2\mathbf{H}(\omega)\mathbf{F}(\omega) \tag{4}$$

The transmissibility function $T_{ij}(\omega)$ between the output DOF i and reference-output DOF j is defined as the ratio between two frequency spectra $A_i(\omega)$ and $A_j(\omega)$. Letting $\mathbf{h}_i(\omega)$ be the i-th row of $\mathbf{H}(\omega)$ and $\mathbf{h}_j(\omega)$ be the j-th row, the transmissibility function $T_{ij}(\omega)$ can be calculated as:

$$T_{ij}(\omega) = \frac{A_i(\omega)}{A_j(\omega)} = \frac{-\omega^2 \mathbf{h}_i(\omega)\mathbf{F}(\omega)}{-\omega^2 \mathbf{h}_j(\omega)\mathbf{F}(\omega)} = \frac{\mathbf{h}_i(\omega)\mathbf{F}(\omega)}{\mathbf{h}_j(\omega)\mathbf{F}(\omega)} \tag{5}$$

If the input force is only applied to the *k*-th DOF, $T_{ij}(\omega)$ is further simplified by substituting Equation (3) into Equation (5):

$$T_{ij}(\omega) = \frac{H_{ik}(\omega)}{H_{jk}(\omega)} \tag{6}$$

where $H_{ik}(\omega)$, $H_{jk}(\omega)$ are entries of the FRF matrix. Therefore, the transmissibility function is determined by the inherent structural property, and is independent from the magnitude of the input force $f_k(t)$. For calculating the transmissibility function $T_{ij}(\omega)$, only the acceleration measurements at DOF *i* and DOF *j* are needed to perform the division between two frequency spectra (Equation(5)). In other words, the input force measurement is not required for determining $T_{ij}(\omega)$ through experiments.

3.2. Definitions of damage indicator and repeatability indicator

Based upon the transmissibility function $T_{ij}(\omega)$, an integral damage indicator (*DI*) between the DOF *i* and DOF *j* is defined as:

$$DI_{ij} = \frac{\int_{\omega_1}^{\omega_2} \left| \ln \left| T_{ij}^U \right| - \ln \left| T_{ij}^D \right| \right| d\omega}{\int_{\omega_1}^{\omega_2} \left| \ln \left| T_{ij}^U \right| \right| d\omega} \tag{7}$$

where superscript *U* and *D* represent the undamaged structure and the damaged structure, respectively. Accordingly, T_{ij}^U and T_{ij}^D represent the transmissibility function of the undamaged structure and the damaged structure, respectively; ω_1 and ω_2 are the lower and upper boundaries of the interested frequency span. If the damage indicators between two DOFs are large, it is likely that structural damage has occurred near these two DOFs.

In order to reduce the effect of experimental uncertainties, the measurement at each configuration is usually repeated for multiple times, with either the undamaged or the damaged structure. If there are *N* repeating experiments, the averaged transmissibility functions are calculated for computing the damage indicator:

$$T_{ij}^U = \frac{1}{N} \sum_{k=1}^{N} (T_{ij}^U)_k \tag{8a}$$

$$T_{ij}^D = \frac{1}{N} \sum_{k=1}^{N} (T_{ij}^D)_k \tag{8b}$$

where the subscript *k* represents the *k*-th repeating test.

Furthermore, experimental repeatability check can be performed to ensure that experimental uncertainties, including sensor noise and the application of external input, have negligible influence to the damage detection results. For either an undamaged or a damaged structure, again assume that the experiment is repeated for *N* times at each pair of DOFs. The *N* data sets are then separated into two groups of *N*/2 data sets. The separation can be simply made according to the sequence numbers of each data set, i.e. data sets with odd sequence numbers constitute one group, and data sets with even sequence numbers constitute another group. Taking the undamaged structure as an example, the averaged transmissibility function of each data group is calculated as:

$$T_{ij}^{U\_odd} = \frac{2}{N}\sum_{k=1}^{N/2}(T_{ij}^{U})_{2k-1} \tag{9a}$$

$$T_{ij}^{U\_even} = \frac{2}{N}\sum_{k=1}^{N/2}(T_{ij}^{U})_{2k} \tag{9b}$$

The repeatability indicator (*RI*) is then defined in a similar form to the damage indicator. For the experiments with the undamaged structure, the repeatability indicator for the DOF pair *i* and *j* is defined as:

$$RI_{ij}^{U} = \frac{\int_{\omega_1}^{\omega_2}\left|\ln\left|T_{ij}^{U\_odd}\right| - \ln\left|T_{ij}^{U\_even}\right|\right| d\omega}{\int_{\omega_1}^{\omega_2}\left|\ln\left|T_{ij}^{U\_odd}\right|\right| d\omega} \tag{10}$$

Note that a smaller repeatability indicator *RI* represents a higher level of repeatability. Similarly, for the experiments with the damaged structure, the averaged transmissibility functions of two data groups can be calculated as $T_{ij}^{D\_odd}$ and $T_{ij}^{D\_even}$. In addition, the repeatability indicator for experiments with the damaged structure, RI_{ij}^{D}, can be calculated.

4. Laboratory experiments

This section first describes the laboratory structure and the dynamic testing scheme. Transmissibility function analysis is conducted to the undamaged structure. Next, two damage scenarios are investigated, the first scenario simulated with an extra mass block, and the second scenario simulated with loosened bolts. Damage detection and localization are successfully conducted for each scenario.

4.1. Experimental setup

A 2D laboratory steel portal frame is constructed for investigating structural damage detection using mobile sensing nodes (Figure 5a). The span of the portal frame is 1.524 m (5 ft), and the height is 0.914 m (3 ft). The beam and two columns have the same rectangular section area of 0.152 m (6 in) × 0.0048 m (3/16 in). Hinge connections are adopted at the bases of the two columns. Each column is connected with the beam through an angle plate, with four bolts on the beam and four bolts on the column. For the undamaged structure, the torque of all bolts is originally set at 13.56Nm (120 lbs-in).

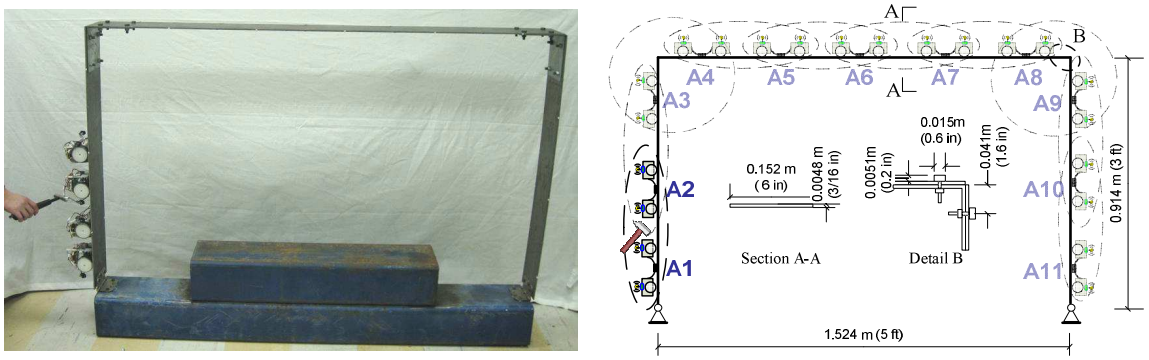

(a) (b)

Figure 5. Laboratory steel portal frame for damage detection using mobile sensing nodes: (a) picture of the portal frame with two mobile nodes at A1 and A2; (b) schematic of sensor and impact locations, undimmed part shows hammer impact being applied between A1 and A2.

Three acceleration measurement locations are assigned on the left (A1 to A3) and right (A9 to A11) columns, respectively. Five acceleration measurement locations (A4 to A8) are uniformly assigned on the beam (Figure 5b). Two mobile sensing nodes are used in the experiments. Each mobile sensing node carries a Silicon Designs 2260-010 accelerometer that has a nominal bandwidth of 0 ~ 1000Hz. On the structure, the two mobile sensing nodes move to each of ten location pairs (e.g. A1-A2, A2-A3, …, A10-A11) to take acceleration measurements. When the two mobile sensing nodes arrive at one pair of measurement locations, the accelerometer is attached onto the structural surface; then a hammer impact is applied at the middle of these two adjacent measurement locations. The acceleration measurement direction is perpendicular to the beam or column surface where the accelerometer is attached. The sampling rate for the acceleration measurement is set to 2500 Hz. Time synchronization between two mobile nodes is achieved by a wireless beacon broadcasted by the server. The synchronization accuracy is about 20μs at the beginning of the measurement [10].

Figure 6(a) plots the acceleration data at location A1 and Figure 6(b) plots the acceleration data at location A2; both data sets are simultaneously collected when an impact hammer hits between A1 and A2. Figure 7 shows the magnitude of the two frequency spectra, i.e. the fast Fourier transform (FFT) results of the acceleration time history. Eight-times zero padding is performed to the time history, in order to achieve a frequency resolution of 0.125 Hz in the spectra. The 0 ~ 100 Hz range of the frequency spectra contains many low valleys that are susceptible to sensor noise. According to the definition, transmissibility function is calculated by the ratio between the two frequency spectra (Equation (5)). If small numerical values exist near the valleys of the denominator spectrum, the division process results in random peaks in the calculated transmissibility function. These random peaks, in turn, cause the damage indicators to be unreliable. To reduce the sensor noise effect, the 0 ~ 100 Hz range of the frequency spectra is not used for calculating the transmissibility function. Instead, the 100 ~ 1,000 Hz frequency range is used, i.e. ω_1 is set to 100 Hz and ω_2 is set to 1,000 Hz in Equation (7).

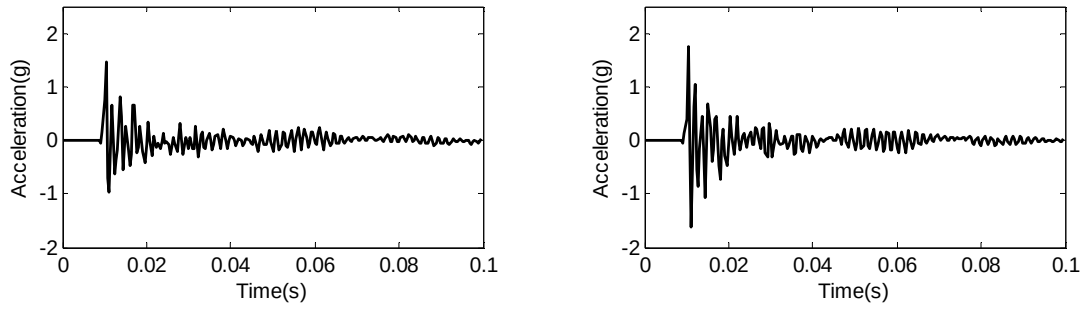

(a) (b)

Figure 6. Acceleration data recorded by mobile sensing nodes: (a) location A1; (b) location A2. Hammer impact is applied between A1 and A2 (as shown in Figure 5b).

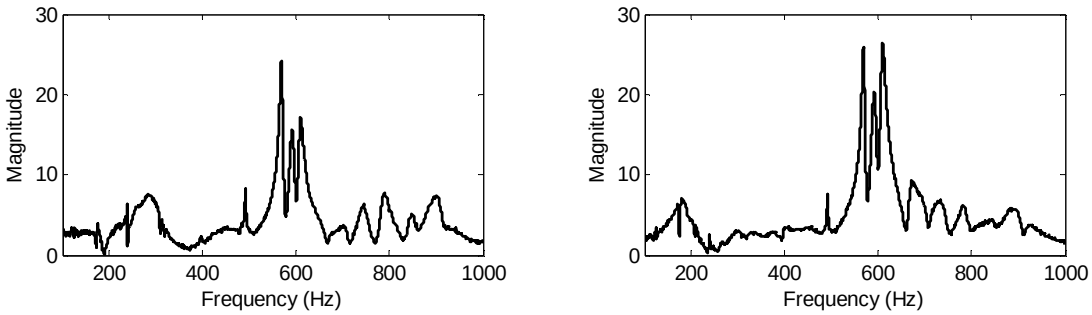

(a) (b)

Figure 7. Frequency spectra of the mobile sensing data in Figure 6: (a) location A1; (b) location A2.

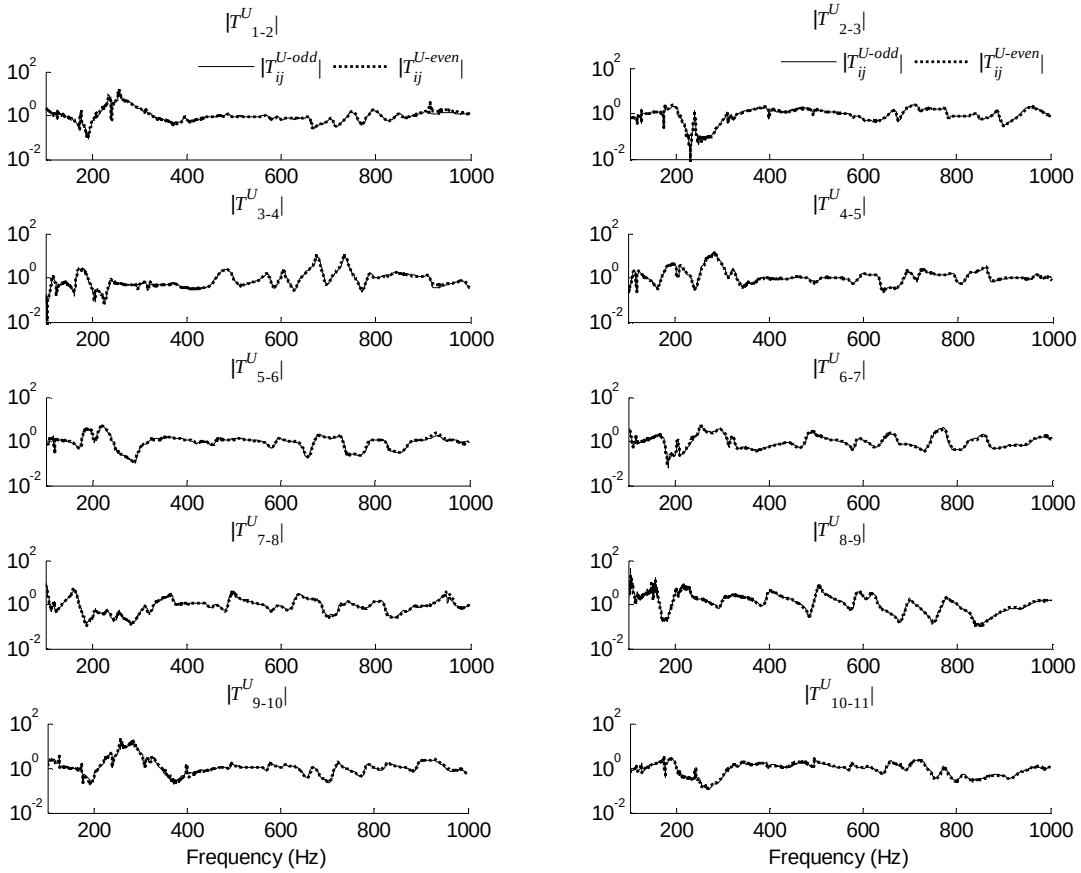

Figure 8. Repeatability of transmissibility functions among data sets for undamaged structure.

In order to reduce the effect of experimental uncertainties, the hammer impact experiments for each location pair is repeatedly conducted for 20 times, i.e. $N = 20$ in Equation (8). The repeatability of the experiments is verified by comparing among the 20 data sets collected from the undamaged structure. The 20 acceleration data sets collected for each pair of locations are separated into two groups of 10 data sets. The separation is simply made according to the sequence numbers of each data set, i.e. data sets with odd sequence numbers constitute one group, and data sets with even sequence numbers constitute another group. Following Equation (9), $T_{ij}^{U\_odd}$ and $T_{ij}^{U\_even}$ are calculated for $i = 1, \ldots 10$ and $j = i + 1$, and the magnitude results are plotted in Figure 8. Due to the random nature of laboratory experiments, minor differences exist between the transmissibility functions calculated from the two groups of data sets. Nevertheless, the $T_{ij}^{U\_odd}$ plots generally match closely with the $T_{ij}^{U\_even}$ plots for all location pairs, which demonstrate reasonable repeatability of the experiments.

4.2. Damage Scenario I – extra mass block

In Damage Scenario I, a steel mass block of 0.575 kg (1.27 lbs) is bonded to the left column for simulating a reversible damage. In contrast, the mass of the left column is 4.985 kg (10.99 lbs). The bonding location is at 0.229 m (9 in) above the column base, which is between locations A1 and A2 (Figure 9). With the mass block bonded at this position, the two mobile sensing nodes sequentially conduct measurements at location pairs A1-A2, A2-A3, and so on. Same as the measurement scheme for the undamaged structure, at each location pair, the hammer impact experiments are repeated for 20 times. The experimental repeatability is verified by separating the 20 data sets at each location pair into an odd-sequence group and an even-sequence group, so that $T_{ij}^{D\_odd}$ and $T_{ij}^{D\_even}$ are calculated. For each location pair, the results demonstrate similar agreement as shown in the repeatability check

for the undamaged structure, i.e. the $T_{ij}^{U\_odd}$ and $T_{ij}^{U\_even}$ plots in Figure 8. Due to page limit, the $T_{ij}^{D\_odd}$ and $T_{ij}^{D\_even}$ plots are not presented.

Figure 9. Damage Scenario I – an extra mass block and two mobile sensing nodes, one node allocated at location A1, and the other node at A2 (locations A1 and A2 are as shown in Figure 5b).

With all the experimental data sets for both the undamaged and damaged structures, according to Equation (8), the averaged transmissibility functions T_{ij}^{U} and T_{ij}^{D} are computed for i = 1, … 10 and j = i + 1. Figure 10 presents the magnitude of the averaged transmissibility functions of both the undamaged structure and the damaged structure (i.e. with the extra mass block). It is shown that the extra mass block changes the amplitude and peak frequencies of the transmissibility functions. In

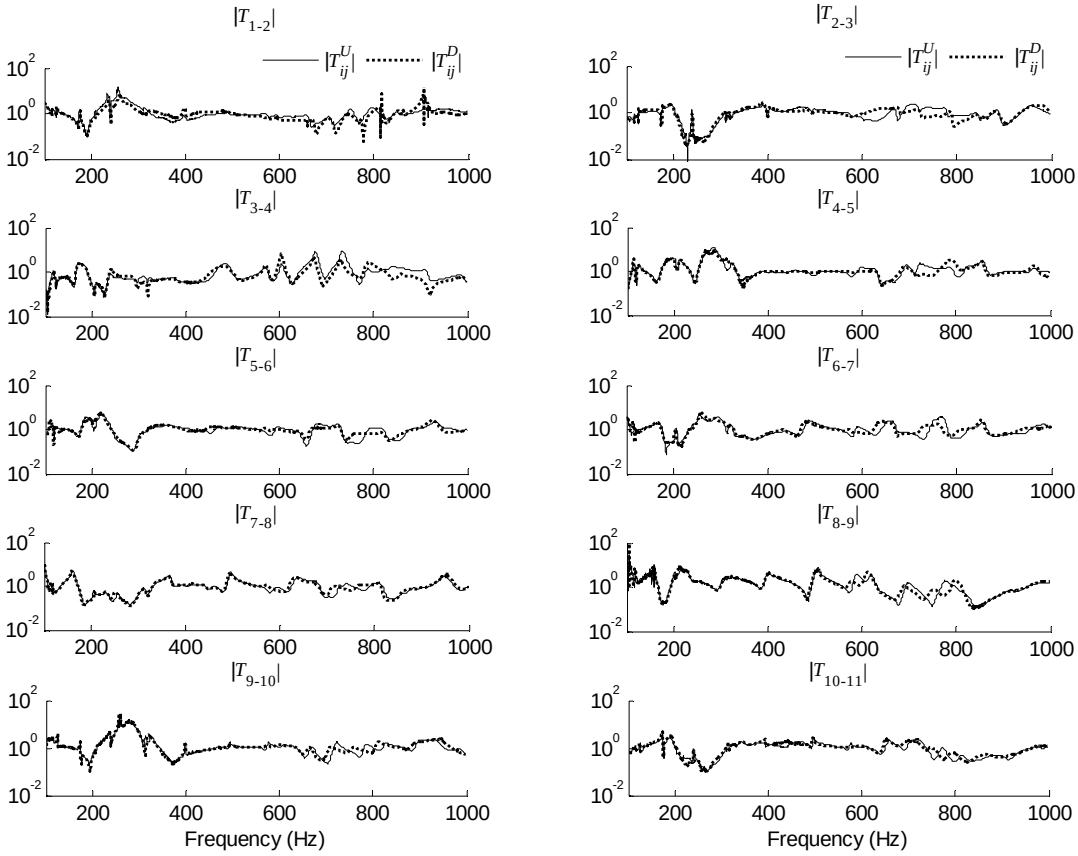

Figure 10. Damage Scenario I – comparison of transmissibility functions between data sets of the undamaged and damaged structures.

particular, larger difference in the transmissibility functions (e.g. $T_{1\text{-}2}$ and $T_{2\text{-}3}$) is observed for location pairs close to the damage location, i.e. the mass block position between A1 and A2. Transmissibility functions (e.g. $T_{8\text{-}9}$ and $T_{9\text{-}10}$) at locations far away from the damage generally demonstrate very little change between the undamaged and damaged structures. Furthermore, the comparison between Figure 8 and Figure 10 shows that difference among $T_{ij}^{U\_odd}$ and $T_{ij}^{U\_even}$ (in Figure 8) is much less than the difference between T_{ij}^{U} and T_{ij}^{D} (Figure 10). This again confirms that the experimental uncertainties are within an acceptable level.

Based upon the averaged transmissibility functions T_{ij}^{U} and T_{ij}^{D}, damage indicators are calculated following Equation (7). The damage indicators basically measure the level of difference between the averaged transmissibility functions of the undamaged structure and of the damaged structure, at each location pair. As presented in Figure 11, the largest damage indicator is $DI_{1\text{-}2} = 0.73$, which agrees with the correct damage location. In general, lower damage indicators are observed for location pairs far away from the damage location. Following Equation (10), repeatability indicators are also calculated for the experiments with the undamaged structure, as well as the experiments with the damaged structure. Note that a smaller repeatability indicator *RI* represents a higher level of repeatability. Figure 11 shows that among all the pairs of measurement locations, the largest repeatability indicator for the data sets of the undamaged structure is $RI_{1-2}^{U} = 0.12$. Among all the pairs of measurement locations, the largest repeatability indicator for the damaged structure is $RI_{5-6}^{D} = 0.14$. Compared with the damage indicators *DI*, the small values of repeatability indicators RI^{U} and RI^{D} demonstrate that the experimental results are reasonably repeatable, and the experimental uncertainties have limited effects to the damage detection.

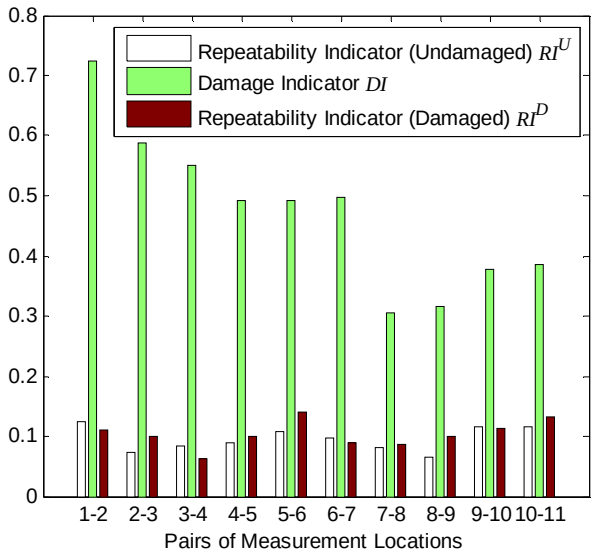

Figure 11. Damage Scenario I – the damage indicators and repeatability indicators for ten pairs of measurement locations.

4.3. Damage Scenario II – loosened bolts

In Damage Scenario II, four bolts at the upper left corner of the steel frame are loosened (Figure 12). The bolts connect the left end of the beam with the angle plate. The torque of each of the four bolts is reduced from 13.56Nm (120 lbs-in) to 0.565Nm (5lbs-in).

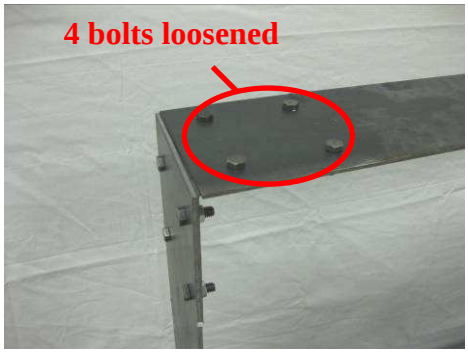

Figure 12. Damage Scenario II – the torque of each of the four bolts is reduced from 13.56Nm (120 lbs-in) to 0.565Nm (5lbs-in). The bolts are between locations A3 and A4 shown in Figure 5(b).

At each location pair, the hammer impact experiments are again repeated for 20 times. Figure 13 compares the magnitude of the averaged transmissibility functions of the undamaged structure and the damaged structure. The transmissibility function at location pair A3-A4 ($T_{3\text{-}4}$) shows the largest difference between the damaged and undamaged structures, which corresponds to the correct damage location. Figure 14 shows the damage indicators as well as repeatability indicators of both undamaged and damaged structures. The largest damage indicator is $DI_{3\text{-}4} = 0.56$, and the location pair A3 and A4 is the correct damage location where bolts are loosened. In addition, all repeatability indicators of the experiments for the undamaged and damaged structure are close to 0.1. These small repeatability indicators again verify that the experimental uncertainties have limited effects to damage detection.

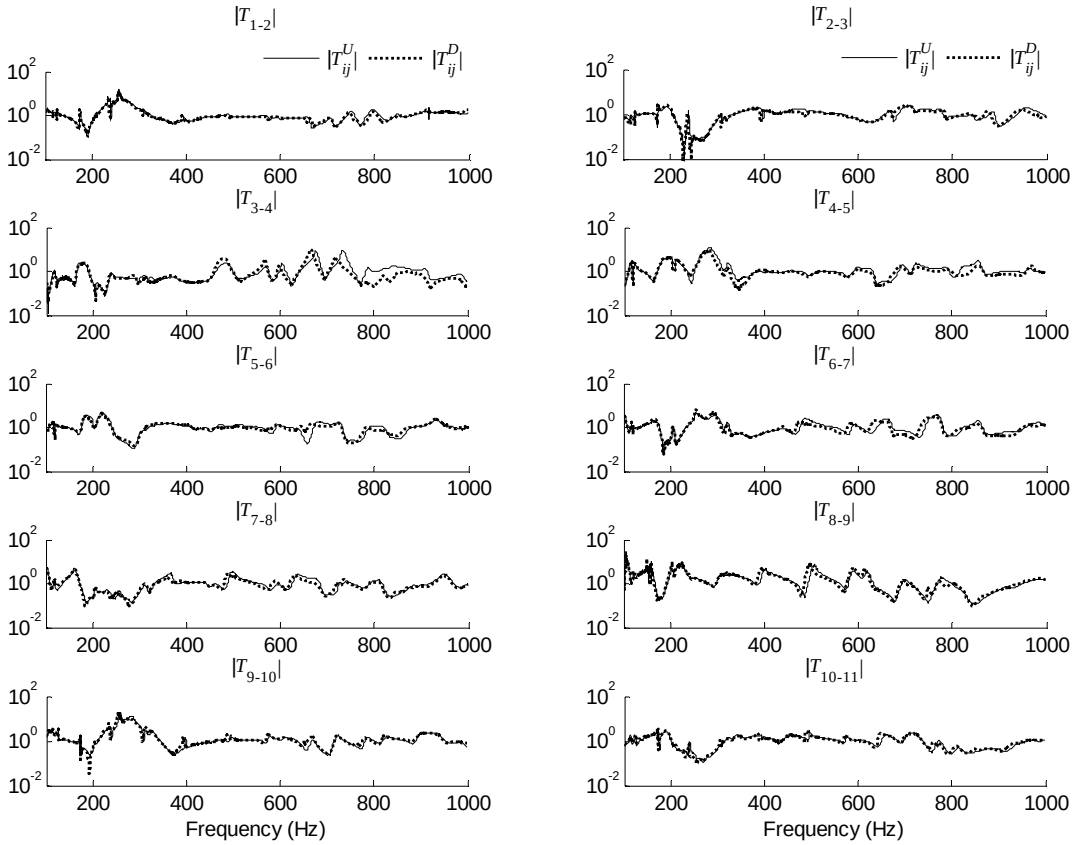

Figure 13. Damage Scenario II: comparison of transmissibility functions between data sets of the undamaged and damaged structures.

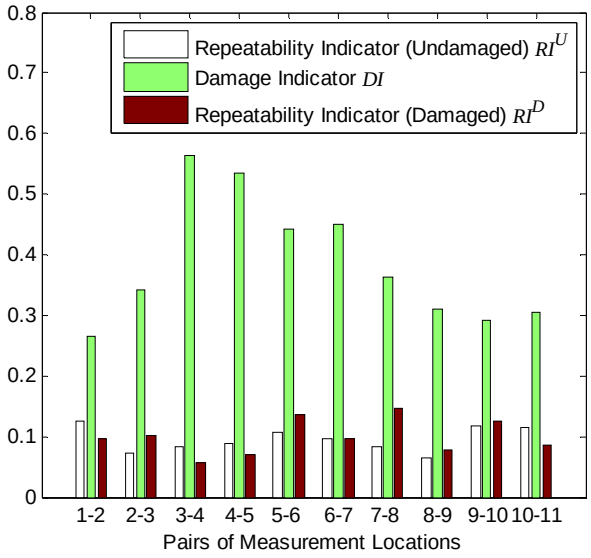

Figure 14. Damage Scenario II – the damage indicators and repeatability indicators for ten pairs of measurement locations.

5. Summary and discussion

This study explores mobile sensors for the structural damage detection of a laboratory portal frame. Tetherless mobile sensors are developed for autonomous maneuvering upon steel structures, and for automatically attaching/detaching accelerometers onto/from the structural surface. A laboratory portal frame is constructed to validate the capability of the mobile sensors in damage detection. Two damage scenarios are investigated, the first scenario simulated with an extra mass block, and the second scenario simulated with four loosened bolts. Using acceleration data collected by the mobile sensors, location of the damage is accurately determined in both scenarios through transmissibility function analysis. The advantage of mobile sensors is thus demonstrated as the high spatial resolution measurement that requires limited number of sensors and little human effort. Such advantage will allow mobile sensor networks to bring transformative changes to future structural health monitoring.

The mobile sensing node presented in this paper is developed for a proof-of-concept study in the laboratory. Significant efforts will be needed for the system to operate reliably in actual civil structures, particularly for the mobile sensing nodes to freely maneuver on 3D structure and overcame complex obstacles. Multi-functional mobile sensing nodes will be developed, so that various physical stimuli can be measured and recorded. For example, wireless cameras can be equipped on future generation of mobile sensing nodes, to allow the mobile sensing nodes to observe their surroundings. In addition, a mobile excitation node can be developed for applying small-magnitude impact forces to one local area of a structure.

Acknowledgement

This research is partially sponsored by the National Science Foundation, under grant number CMMI-0928095 (Program Manager: Dr. Shih-Chi Liu). The authors gratefully acknowledge the support.

References

[1] ASCE 2009 *Report Card for America's Infrastructure* (Reston, VA: American Society of Civil Engineers)

[2] Moore M, Phares B, Graybeal B, Rolander D and Washer G 2001 *Reliability of Visual Inspection for Highway Bridges* Report No. FHWA-RD-01-020 (McLean, VA: Federal Highway Administration)
[3] Farrar C R, Sohn H, Hemez F M, Anderson M C, Bement M T, Cornwell P J, Doebling S W, Schultze J F, Lieven N and Robertson A N 2003 *Damage Prognosis: Current Status and Future Needs* Report No. LA-14051-MS (Los Alamos, NM: Los Alamos National Laboratory)
[4] Glaser S D, Li H, Wang M L, Ou J and Lynch J P 2007 *Smart Struct. Syst.* **3** 221-44
[5] Straser E G and Kiremidjian A S 1998 A Modular, *Wireless Damage Monitoring System for Structures* Report No. 128 (Stanford, CA: John A. Blume Earthquake Eng. Ctr., Stanford University)
[6] Lynch J P and Loh K J 2006 *Shock Vib. Dig.* **38** 91-128
[7] Kim S, Pakzad S, Culler D, Demmel J, Fenves G, Glaser S and Turon M 2007 Health monitoring of civil infrastructures using wireless sensor networks. *Proceedings of the 6th International Conference on Information Processing in Sensor Networks (IPSN '07)* (Cambridge, MA)
[8] Spencer B F, Jr., Ruiz-Sandoval M E and Kurata N 2004 *Struct. Control Hlth.* **11** 349-68
[9] Shinozuka M, Feng M Q, Chou P, Chen Y and Park C 2004 MEMS-based wireless real-time health monitoring of bridges. *Proceedings of the 3rd International Conference on Earthquake Engineering* (Nanjing, China)
[10] Wang Y, Lynch J P and Law K H 2007 *Struct. and Infrastructure Eng.* **3** 103-20
[11] Wang Y, Loh K J, Lynch J P, Fraser M, Law K H and Elgamal A 2006 Vibration monitoring of the Voigt Bridge using wired and wireless monitoring systems. *Proceedings of the 4th China-Japan-US Symposium on Structural Control and Monitoring* (Hangzhou, China)
[12] Lynch J P, Wang Y, Loh K J, Yi J-H and Yun C-B 2006 *Smart Mater. Struct.* **15** 1561-75
[13] Weng J-H, Loh C-H, Lynch J P, Lu K-C, Lin P-Y and Wang Y 2008 *Eng. Struct.* **30** 1820-30
[14] Akyildiz I F, Su W, Sankarasubramaniam Y and Cayirci E 2002 *IEEE Commun. Mag.* **40** 102-14
[15] LaMarca A, Brunette W, Koizumi D, Lease M, Sigurdsson S B, Sikorski K, Fox D and Borriello G 2002 Making sensor networks practical with robots. *Proceedings of the First International Conference on Pervasive Computing* (Zurich, Switzerland)
[16] Dantu K, Rahimi M, Shah H, Babel S, Dhariwal A and Sukhatme G 2005 Robomote: enabling mobility in sensor networks. *Proceedings of the 4th International Symposium on Information Processing in Sensor Networks (IPSN)* (Los Angeles, CA)
[17] Backes P G, Bar-Cohen Y and Joffe B 1997 The multifunction automated crawling system (MACS). *Proceedings of the 1997 IEEE International Conference on Robotics and Automation* (Albuquerque, New Mexico) vol 1
[18] Huston D R, Esser B, Gaida G, Arms S W and Townsend C P 2001 Wireless inspection of structures aided by robots. *Proceedings of SPIE, Health Monitoring and Management of Civil Infrastructure Systems* (Newport Beach, CA) vol 4337
[19] Brian E, Jon M, Dryver R H and Phil B 2004 Robotic systems for homeland security. *Proceedings of SPIE, Nondestructive Detection and Measurement for Homeland Security II* (San Diego, CA) vol 5395
[20] Todd M, Mascarenas D, Flynn E, Rosing T, Lee B, Musiani D, Dasgupta S, Kpotufe S, Hsu D, Gupta R, Park G, Overly T, Nothnagel M and Farrar C 2007 A different approach to sensor networking for SHM: remote powering and interrogation with unmanned aerial vehicles. *Proceedings of the 6th International Workshop on Structural Health Monitoring* (Stanford, CA)
[21] Zhu D, Qi Q, Wang Y, Lee K-M and Foong S 2009 A prototype mobile wireless sensor network for structural health monitoring. *Proceedings of SPIE, Nondestructive*

Characterization for Composite Materials, Aerospace Engineering, Civil Infrastructure, and Homeland Security 2009 (San Diego, CA) vol 7294
[22] Lee K-M, Wang Y, Zhu D, Guo J and Yi X 2009 Flexure-based mechatronic mobile sensors for structure damage detection. *Proceedings of the 7th International Workshop on Structural Health Monitoring* (Stanford, CA, USA)
[23] Guo J, Lee K-M, Zhu D and Wang Y 2009 A flexonic magnetic car for ferro-structural health monitoring. *Proceedings of 2009 ASME Dynamic Systems and Control Conference* (Hollywood, CA)
[24] Kess H R and Adams D E 2007 *Mech. Syst. Signal Pr*. **21** 2394-405
[25] Johnson T J and Adams D E 2002 *J. Vib. Acoust.* **124** 634-41
[26] Zhang H, Schulz M J, Ferguson F and Pai P F 1999 *Mech. Syst. Signal Pr.* **13** 765-87
[27] Devriendt C, De Sitter G, Vanlanduit S and Guillaume P 2009 *Mech. Syst. Signal Pr.* **23** 621-35
[28] Çelebi M 2002 *Seismic Instrumentation of Buildings (with Emphasis on Federal Buildings)* Report No. 0-7460-68170 (Menlo Park, CA: United States Geological Survey)
[29] Doebling S W, Farrar C R and Prime M B 1998 *Shock Vib. Dig.* **30** 91-105